



## The 2<sup>nd</sup> measurement campaign of the Medicina Array Demonstrator

VERSION 2.1

*G. Pupillo<sup>1</sup>, G. Naldi<sup>1</sup>, A. Mattana<sup>1</sup>,  
J. Monari<sup>1</sup>, F. Perini<sup>1</sup>, M. Schiaffino<sup>1</sup>,  
P. Bolli<sup>2</sup>, G. Virone<sup>3</sup>, A. Lingua<sup>4</sup>*

Referee: M. Poloni<sup>1</sup>

**IRA 479/14**

(1) *Istituto di Radioastronomia di Bologna – INAF*

(2) *Osservatorio Astrofisico di Arcetri - INAF*

(3) *IEIIT - CNR di Torino*

(4) *DIATI - Politecnico di Torino*

## Index

|   |    |
|---|----|
| 1 - Introduction.....                           | 2  |
| 2 - Medicina Array Demonstrator.....            | 3  |
| 2.1 - Array configuration and location.....     | 3  |
| 2.2 - Antennas deploying / positioning .....    | 4  |
| 2.3 – Array photogrammetry.....                 | 6  |
| 2.4 – Digital backend .....                     | 7  |
| 2.4.1 – Firmware Architecture Description ..... | 7  |
| 2.4.2 – Integration time.....                   | 10 |
| 2.4.3 – ADC Crosstalk Lab Tests.....            | 11 |
| 3 – Description of the UAV .....                | 12 |
| 4 – Analogue signal equalization .....          | 14 |
| 5 – Amplitude calibration .....                 | 15 |
| 6 – Phase calibration .....                     | 17 |
| 7 – Embedded element patterns.....              | 20 |
| 8 – Array beam .....                            | 26 |
| 9 – Conclusions .....                           | 28 |
| 10 – List of abbreviations .....                | 29 |
| 11 – References .....                           | 29 |
| 12 – Appendix A.....                            | 30 |

## 1 - Introduction

This report summarizes the main results of the second MAD measurement campaign (MAD-2) carried out on 17<sup>th</sup>-18<sup>th</sup> October 2013. The aim of the test was to verify the use of an Unmanned Aerial Vehicle (UAV) as source in far-field for characterization and calibration of small low-frequency aperture arrays in their operative conditions (e.g. on the ground, with mutual coupling effects, etc.). The array under test was the Medicina Array Demonstrator, a small low-frequency array installed inside the area of the Medicina radioastronomical station. The MAD-2 campaign was performed in the framework of the SKA-LFAA program.

The MAD-2 campaign has been preceded by two other test sessions: mini-MAD and MAD-1. Mini-MAD, carried out on June 2013, was performed using only two elements in order to test a single baseline. Whereas in MAD-1, that took place in July 2013, the full MAD array was tested and debugged for the first time. These preliminary campaigns were very useful to find some critical issues in the backend configuration software, that were fixed before MAD-2 test.

## 2 - Medicina Array Demonstrator

### 2.1 - Array configuration and location

The Medicina Array Demonstrator (MAD) is a 3x3 regularly spaced array composed by Vivaldi v2.0 antennas, operating in dual polarization. The array is arranged in a rhomboidal configuration, as illustrated in Fig. 1.

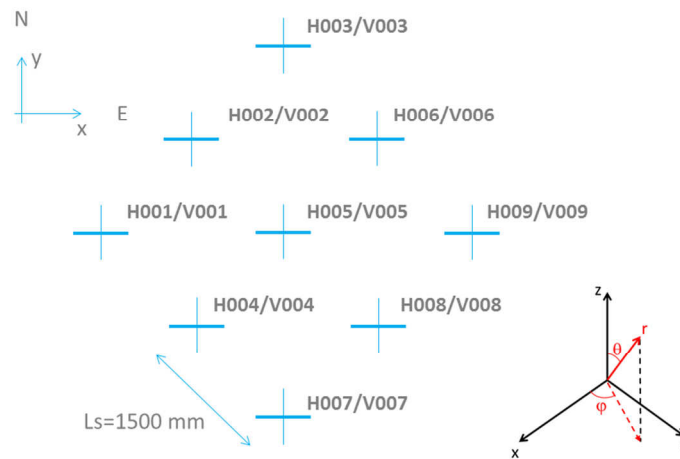


Fig. 1 – Array geometry. Bold and thin lines represent the horizontal and vertical polarization, respectively.

The theoretical antenna positions, expressed in the ENU local reference frame ( $x$ ,  $y$ ,  $z$ -axes toward East, North and Zenith, respectively), are shown in Table 1. The origin of this frame is set in the central element of the array (antenna V005/H005).

| Antenna ID | X (m)    | Y (m)    | Z (m)   |
|------------|----------|----------|---------|
| V001/H001  | -2.12132 | 0.00000  | 0.00000 |
| V002/H002  | -1.06066 | 1.06066  | 0.00000 |
| V003/H003  | 0.00000  | 2.12132  | 0.00000 |
| V004/H004  | -1.06066 | -1.06066 | 0.00000 |
| V005/H005  | 0.00000  | 0.00000  | 0.00000 |
| V006/H006  | 1.06066  | 1.06066  | 0.00000 |
| V007/H007  | 0.00000  | -2.12132 | 0.00000 |
| V008/H008  | 1.06066  | -1.06066 | 0.00000 |
| V009/H009  | 2.12132  | 0.00000  | 0.00000 |

Table 1 – Ideal ENU positions of the MAD array elements

MAD has been installed inside the Medicina radioastronomical station area, near to the NS arm of the Northern Cross antenna (Fig. 2). This location allowed the utilization of both the station infrastructures and the already installed BEST-2 receiving chains. For the latter reason the operative frequency in the MAD-2 campaign was 408 MHz, although the Vivaldi 2.0 antenna covers a frequency range from 70 to 450 MHz.

However two big scatterers were quite close to the array and then influenced the array/antenna patterns: the huge metallic structure of the Northern Cross antenna and a power line.

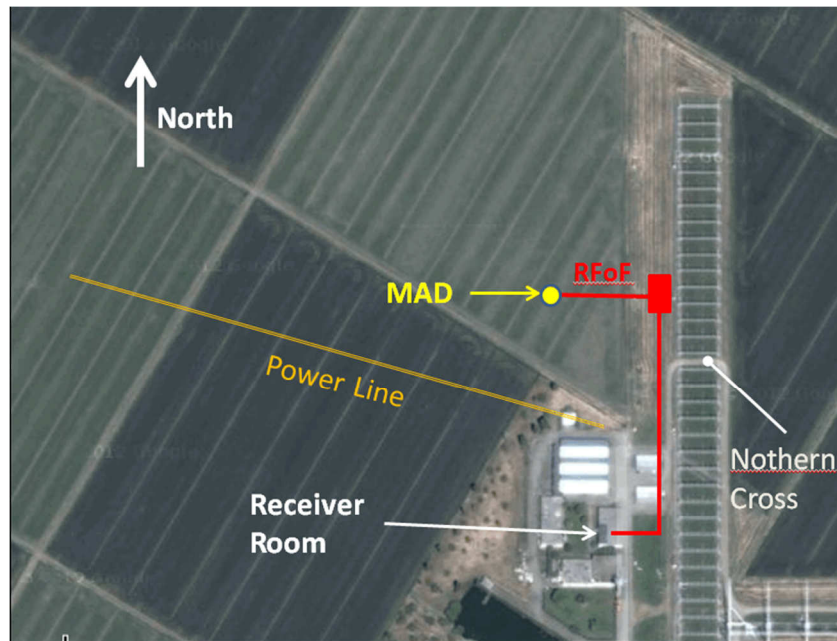


Fig. 2 – Aerial view of the MAD location area inside the Medicina radioastronomical station

## 2.2 - Antennas deploying / positioning

Before the antenna deploying, the ground has been prepared and levelled. The procedure for the positioning of the 9 Vivaldi antennas has been the following:

- Total station measures the absolute positions of 4 reference stakes forming a rectangle on the ground (yellow rhombs in Fig. 3) aligned with the principal directions;
- A CAD software calculates the vertical and horizontal projections of each antenna center on the sides of the reference rectangle;
- The sides of the rectangle and the antenna projections are formed on the ground by means of a special elastic rope (blue lines in Fig. 3);
- Antenna centers are positioned in the intersection points (red circles in Fig. 3);
- Special templates and adjusting pads are used to define the correct antenna orientation (Fig. 4);
- The array planarity is obtained adjusting each antenna height by a bubble level connected to a long flat aluminum screed;

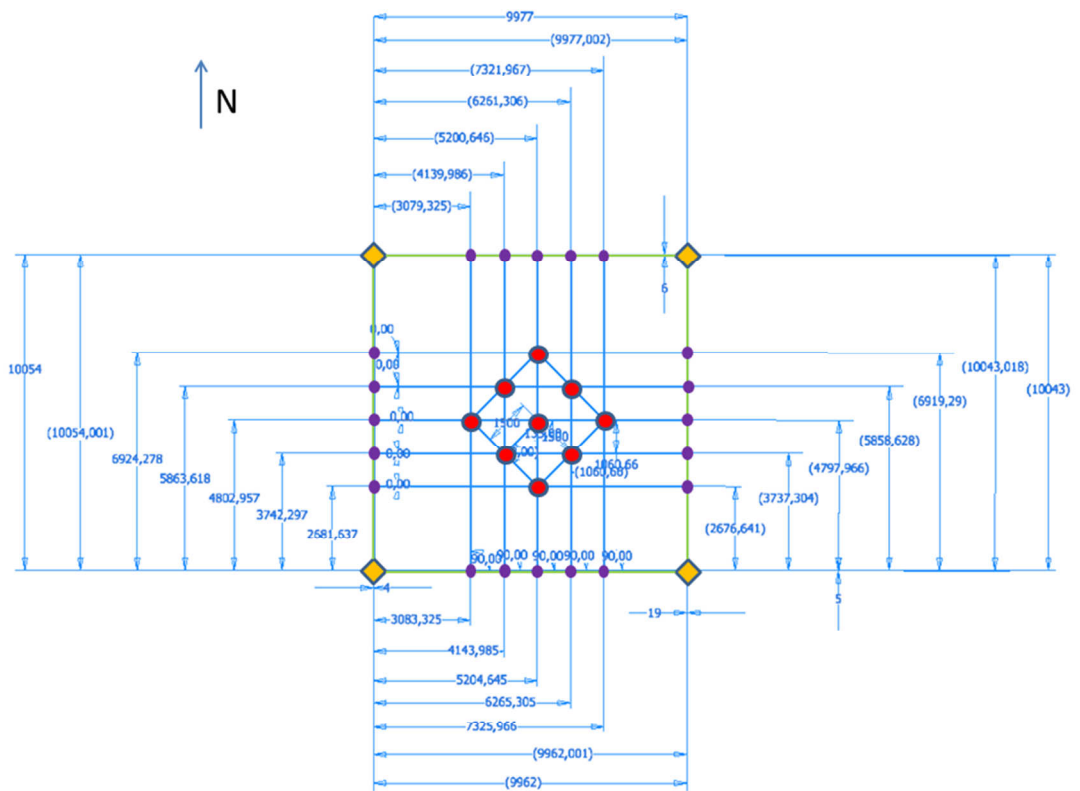


Fig. 3 – Projection of the antenna centers used for the array positioning

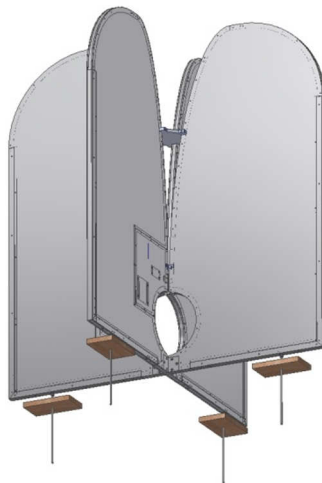


Fig. 4 – 3D view of the four adjusting plates placed under the antenna wings

A first verification of the relative antenna positions have been performed measuring the distances between antenna centers by means of a measuring tape. The relative distance errors result lower than 0.6 cm.

## 2.3 – Array photogrammetry

After the first verification, the antenna positions were measured by a photogrammetric technique based on aerial pictures taken by a high resolution camera installed on the UAV. In order to improve the accuracy of these measurements, an optical target was placed at the top center of the plastic spacer between the wings of the Vivaldi antenna (Fig. 5).

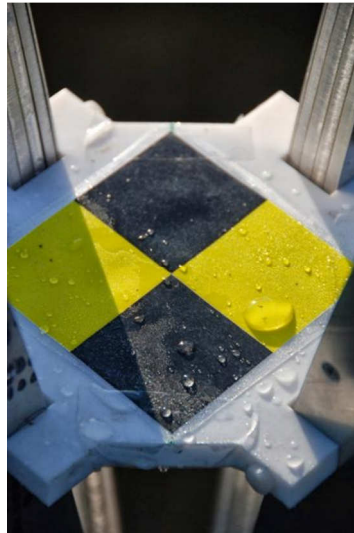


Fig. 5 - Optical maker at top of the Vivaldi wings spacer

A very good agreement between measured and theoretical X and Y coordinates is obtained (see Table 2).

In this comparison Z coordinates (heights) were not taken into account because significant errors affected the photogrammetric heights. However, the measurement precision of the Z coordinates could be greatly improved choosing proper UAV trajectories.

| Antenna ID | X (m)   | Y (m)   | $\Delta X$ (cm) | $\Delta Y$ (cm) |
|------------|---------|---------|-----------------|-----------------|
| V001/H001  | -2,122  | -0,001  | 0,068           | 0,1             |
| V002/H002  | -1,0646 | 1,0597  | 0,394           | 0,096           |
| V003/H003  | -0,0052 | 2,1273  | 0,52            | -0,598          |
| V004/H004  | -1,0604 | -1,0555 | -0,026          | -0,516          |
| V005/H005  | 0       | 0       | 0               | 0               |
| V006/H006  | 1,0513  | 1,0686  | 0,936           | -0,794          |
| V007/H007  | -0,0073 | -2,1227 | 0,73            | 0,138           |
| V008/H008  | 1,0537  | -1,0577 | 0,696           | -0,296          |
| V009/H009  | 2,1111  | 0,0018  | 1,022           | -0,18           |

Table 2 – Photogrammetric X,Y ENU coordinates of the array elements (columns 2,3) and their differences with the corresponding theoretical positions (columns 4,5)

## 2.4 – Digital backend

### 2.4.1 – Firmware Architecture Description

Ad-hoc digital acquisition system has been specifically developed for both correlation and beamforming purposes. The firmware has been designed and synthesized on ROACH1 board, which is a generic FPGA (Field Programmable Gate Array)-based board designed by CASPER2 for radio astronomy applications. The ROACH platform is based on a XILINX Virtex-5 SX95T3 FPGA with interfaces to DRAM and QDR memory, high speed CX-4 connectors and a generic Z-DOK interface for connecting ADCs and various daughter boards. Additionally, the board has a PowerPC running BORPH, a variant of Debian Linux, which allows access to software registers and shared memory on the FPGA. Firmware is designed using MATLAB Simulink which is extended with XILINX DSP blocks and CASPER's open source DSP blocks<sup>4</sup>. Fig. 6 depicts the digital backend with all hardware devices and the relative interconnections.

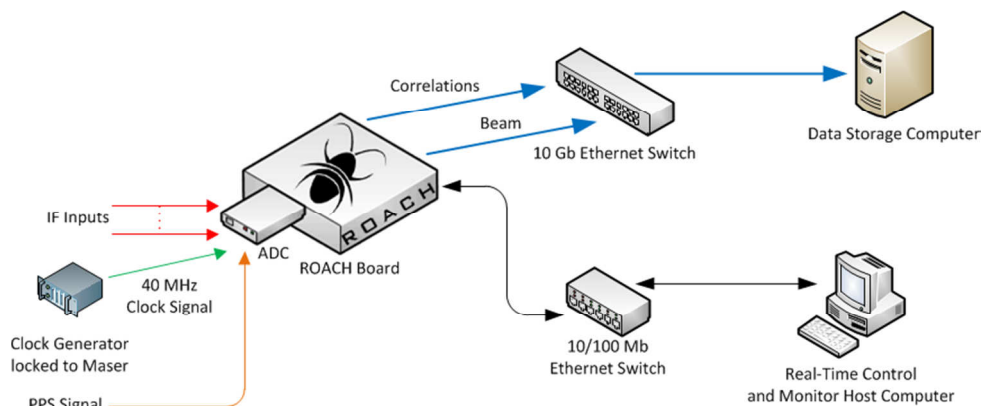


Fig. 6 – Digital backend.

The block diagram in Fig. 7 represents all the signal processing carried out on ROACH (between the AD conversion and the 10 GbE network interface with the data storage computer).

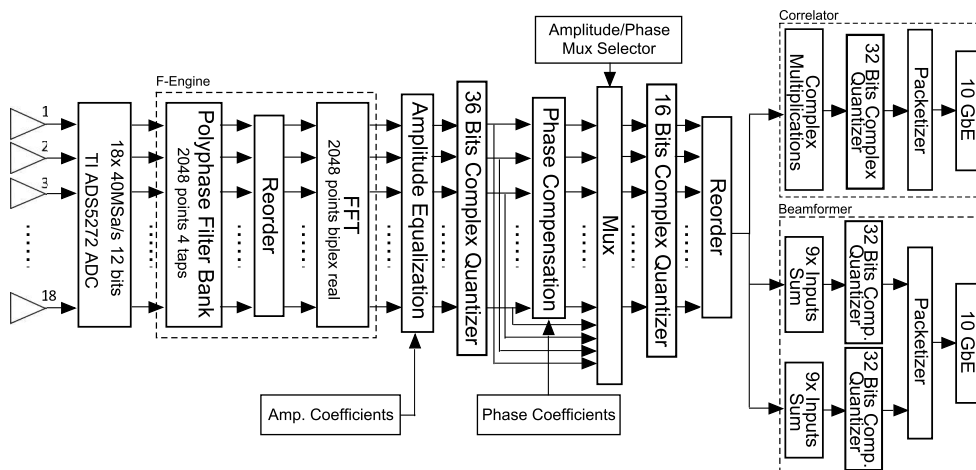


Fig. 7 – Block diagram representing the firmware architecture of the correlator/beamformer systems used for MAD-2 experiment.

<sup>1</sup> Reconfigurable Open Architecture Computing Hardware - <https://casper.berkeley.edu/wiki/ROACH>

<sup>2</sup> <https://casper.berkeley.edu/>

<sup>3</sup> <http://www.xilinx.com/support/documentation/virtex-5.htm>

<sup>4</sup> <https://casper.berkeley.edu/>

Signal digitization is performed using the Texas Instruments ADS5272 8 channel, 12 bit ADC. The ADC board, developed by Rick Raffanti<sup>5</sup>, uses eight ADCs to channelize 64 streams at up to 65 MSPS. In this design only 18 signal streams (9 antennas with dual polarization) are digitized at 40 MSPS which covers the 16 MHz analogue band of the MAD system. The ADC is clocked with a 160 MHz clock locked to a local maser source. During the analogue stage the radio frequency (RF) signal, centered at 408 MHz, is mixed down, with a LO frequency of 378 MHz, to IF frequency (30 MHz). The ADC is connected via a dual Z-DOK interface to the ROACH board, as depicted in Fig. 8.



**Fig. 8 - The ROACH board, a XILINX Virtex-5 SX95T FPGA board, with the 64 input ADC connected via two Z-DOK connectors.**

Both correlator and beamformer share the same “F-engine”, mainly composed by the combination of Polyphase Filter Bank (PFB) and FFT. This block is necessary to perform the frequency channelization of the sampled data. The PFB is a four tap Hann filter bank with 2048 points that produces 1024 samples per real antenna stream. Also FFT is designed with 2048 points for the full complex bandwidth, but only 1024 of these are taken into account because only the real bandwidth is processed. The FFT output is a sequence of samples: each of them belongs to a different frequency channel following a well-defined order. In this way we can pass from time domain to frequency domain. Each frequency channel has a width of 19.5 kHz and the output of the FFT stage is 36 bit complex.

The instrumental calibration in amplitude (equalization) and phase (compensation) is performed through multiplication of the signals with suitable complex gains, which are loaded in the firmware by software routines. After amplitude equalization and phase compensation stages data are scaled and quantized down to 36 bits complex and 16 bits complex respectively. This choice allows to have a good tradeoff between the use of hardware resources, fitting the entire design into Virtex-5 FPGA of the ROACH board, and the correct description of the signal dynamic range.

A multiplexer is available to skip the phase equalization process depending on the mux selector signal. This is useful during the calibration procedure: in fact the first calibration step consists in correlating signals that are equalized only in amplitude (not in phase); in the second step, phase correction coefficients are loaded into FPGA thus they are applied to signals. In this last step the output of the correlator allows to check if the calibration is successfully carried out. For more details about the calibration procedure see section 6.

<sup>5</sup> <https://casper.berkeley.edu/wiki/64ADCx64-12>

The beamformer system works in parallel with the correlator and its output is sent to a data storage computer via 10 GbE network and saved only when data streams from each antenna are calibrated both in amplitude and phase. Basically it calculates separately the sum of the signals of the same polarization, so we have two parallel streams at the output of the beamforming system, one for the vertical polarization and the other for the horizontal polarization. These outputs are the calibrated beams of the two polarizations.

The correlator system calculates the complex multiplications of the couples of antennas relative to a proper subset of not-redundant baselines only (see Table 5). Also it provides the autocorrelations of all antennas. The correlator output is sent to the data storage computer by 10 GbE network.

Similarly to calibration stage, data scaling and quantization is performed both in correlator and beamformer system before packetizing and sending output data to the storage computer. In particular data is quantized down to 32 bits complex in both cases: in this way we have a relatively low output data rate and, at the same time, the signal dynamic range is still correctly described. General backend specifications are summarized in Table 3.

| Digital Back-end Firmware Specifications |                            |                          |
|--|----------------------------|--------------------------|
| ADC Sampling Rate                        | 40                         | Mbps                     |
| ADC Sampling Precision                   | 12                         | bit                      |
| Antenna #                                | 9                          | Dual Pol.                |
| Polarization #                           | 2                          |                          |
| PFB                                      | 4 tap FIR + 2048 point FFT | Radix-2 Biphase Real FFT |
| Frequency resolution                     | 19.5                       | kHz                      |
| Time resolution                          | 51.2                       | $\mu$ s                  |
| Quantization after FFT                   | 36                         | bit                      |
| Quantization after Amplitude Eq.         | 36                         | bit                      |
| Quantization after Phase Eq.             | 16                         | bit                      |
| Correlator                               |                            |                          |
| Auto Correlations                        | 9                          |                          |
| Cross Correlations                       | 8                          |                          |
| Quantization                             | 32                         | bit                      |
| Effective Output Data Rate <sup>6</sup>  | 11.25                      | Mb/s                     |

<sup>6</sup> The effective output data rate is calculated without taking into account of the 8 bytes packet header which depends on the packet size set (~0.02% in the case of MAD-2 set up with 648 as packet length).

| Beamformer                              |      |                    |
|---|------|--------------------|
| Beams                                   | 2    | 1 H Pol., 1 V Pol. |
| Quantization                            | 32   | bit                |
| Effective Output Data Rate <sup>6</sup> | 1.25 | Mb/s               |

Table 3 – Digital backend specifications

### 2.4.2 – Integration time

Data are not integrated aboard the digital backend in order to allow an accurate debug of the acquisition chain and to have a more flexible system, but it produces a large amount of data to be recorded. The data integration is then performed in the post-processing and this allows the optimization of the integration time depending on the hexacopter trajectory, type of operation (calibration, embedded pattern measurement, etc.) and the desired accuracy.

In particular, the hexacopter motion causes errors in the measurements of both phase (fringe smearing) and radiation pattern (pattern blur) that reduce the maximum suitable integration time.

In the radiation pattern measurement, the maximum integration time  $\tau_{max}$  is given by:

$$\tau_{max} = \frac{h}{v} \tan(\Delta\vartheta_{max})$$

In which  $h$  is the height of the hexacopter [m],  $v$  its horizontal speed [m/s] and  $\Delta\vartheta_{max}$  is the maximum allowed angular error in the pattern measurement due to the motion blur.

Whereas, from the phase point of view, the maximum integration time  $\tau_{max}$  in the worst case (zenith) and in the small angle approximation, is:

$$\tau_{max} \cong \frac{h\lambda\Delta\phi_{max}}{2\pi L_{baseline}v}$$

Where  $h$  is the height of the hexacopter [m],  $v$  is the component of the hexacopter speed parallel to the baseline [m/s], the  $L_{baseline}$  the baseline length [m],  $\lambda$  the wavelength [m] and  $\Delta\phi_{max}$  is the maximum allowed phase error [rad] due to the fringe smearing.

In the MAD-2 campaign we choose 3.6 ms integration time (i.e. 70 integrated data samples) that, assuming 1.5 m/s of hexacopter horizontal speed and an height of 60 m, corresponds to about 0.2° phase smearing on the MAD longest baseline and only 0.005° angle error in the pattern measurements.

### 2.4.3 – ADC Crosstalk Lab Tests

Before starting the measurement campaign, a deep analysis on ADC board was performed. We observed that:

- 1) channel crosstalk results to be less than -30dB, so that it can be considered negligible;
- 2) different channels present different noise floors.

These crosstalk measurements (Fig. 9) were accomplished connecting the signal generator to the ADC input H00x or V00y through a coax cable. The synthesizer was set to generate a power ramp at 30 MHz (OL at 377,999712 MHz). The data acquisition started with the output of the signal generator set to RFOff, then the output power was gradually incremented from -35dBm to +10dBm with 1dB of step. While one ADC input was connected to the signal generator, the other inputs were connected to the corresponding MAD receivers (up to 18 inputs of course, the other were connected to the BEST-2 receivers). All the receivers did not receive any power from antennas since batteries were disconnected (in the case of BEST-2 receivers, the optical fibers from the front-ends were not connected). But this does not mean that the signals entering into ADC inputs were null because all the receivers installed in the rack were left on. The measurement of ADC output power is obtained calculating the average of the counts. In the Fig. 9 and Fig. 10, generated from the measurement analysis, the received power on the H001 ADC input is shown when separate subsequent ramps (x-axis is time) are injected into the different ADCs H00X (Fig. 9) and V00X (Fig. 10).

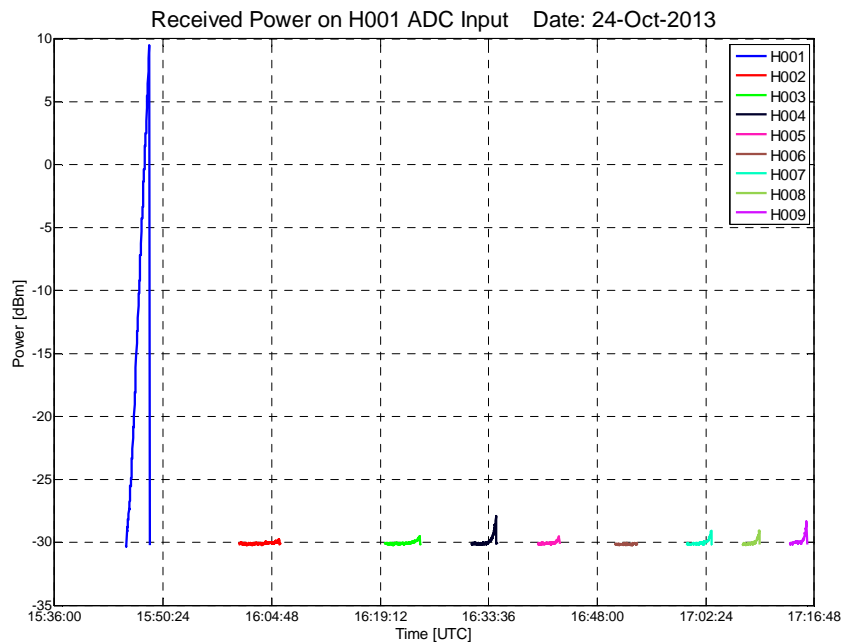


Fig. 9 – Crosstalk measurements on H001 ADC input injecting ramp signal into H00x ADC input

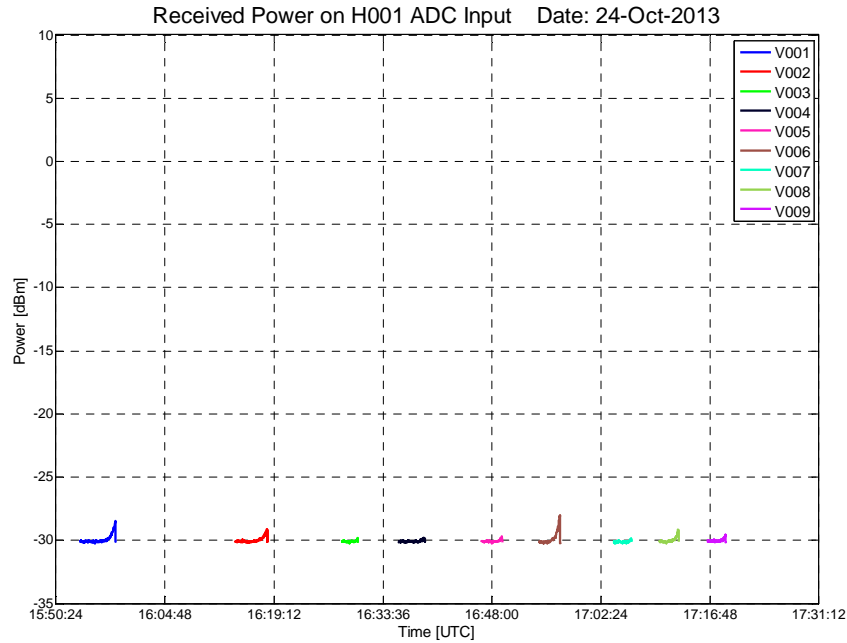


Fig. 10 - Crosstalk measurements on H001 ADC input injecting ramp signal into V00x ADC input

The result of these measurements is that channel crosstalk is present but, even in the worst condition i.e. with  $P_{in}=+10\text{dBm}$ , is less than  $-30\text{dB}$ . So we think that channel crosstalk has a negligible effect on the beamforming output. Moreover a great difference in the noise floor of the various ADC channels is clearly visible. Some channels present a  $-30\text{dBm}$  floor without any input signal, whereas other channels have a  $-38\text{dBm}$  floor. In the future these measurements could be repeated connecting all the ADC inputs to a load matched to  $50\ \Omega$  (or alternatively turning off all the power amplifiers in the IF boards) rather than to the receivers left on (although disconnected from the respective antennas).

As further analysis, another measure could be performed with more than one power supplied input (e.g. 8 out of 9) and verify that phase differences among channels are constant with the variation of the signal amplitude; also it could be important to verify that they are constant with the variation of the number and of the configuration of the power supplied inputs.

For this last point, it would be necessary to verify the effect generated truncating all ADC outputs to a number of bits equal to the worst case ENOB, so that all data streams can work with only significant bits.

### 3 - Description of the UAV

The hexacopter used in the MAD-2 campaign is shown in Fig. 11. Its navigation and control board is a Mikrocopter KGPS v1.0 equipped with the u-blox 6S sensor. It allows a GPS-controlled autonomous flight with a maximum duration of 10-15 minutes (depending on the capacity of the battery, type of flight, wind conditions, etc.). The UAV control board also provides a stable orientation of the hexacopter during the flight. The three orientation angles /bearing, pitch and roll with an accuracy of about  $2^\circ$ . The orientation data were not used for the MAD-2 post-processing.

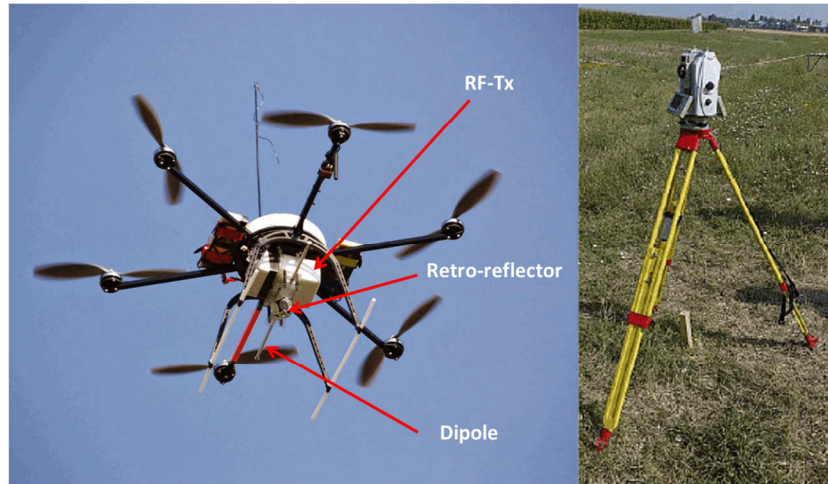


Fig. 11 – (left) Flying hexacopter equipped with RF transmitter, telescopic dipole and optical retroreflector. (right) Motorized total station on the tripod (right)

The hexacopter has been equipped with a continuous-wave RF signal transmitter that can operate from 30M Hz to 900 MHz (with some modifications from 5 MHz to 4.4 GHz) and a telescopic dipole antenna which length can be adjusted for each operative frequency. The optical retroreflector visible in the lower part of the UAV payload has been introduced for accurate optical tracking during the overall flight by means of a motorized total station. This tracking is necessary because the onboard navigation GPS exhibits a metrical accuracy that could not be sufficient for our purposes. The motorized total station Leica 1200+ TCRP 1201 – R 300 measures both distances and angles with accuracies of 3 mm and 1 arcsec, respectively. However the real accuracy during the tracking of the UAV is of the order of 1 cm, that leads to an accuracy of about 0.6 arcmin on the relative observation angle between the UAV and the antenna under test at a flying height of 60 m. Since in MAD the maximum antenna separation is  $D=4.23$  m and the operating frequency is 408 MHz ( $\lambda=0.735$  m), this height is sufficient to fulfill the far-field condition:  $R \geq \frac{2D^2}{\lambda}$ . The far-field condition as function of the frequency for different array sizes is plotted in Fig. 12.

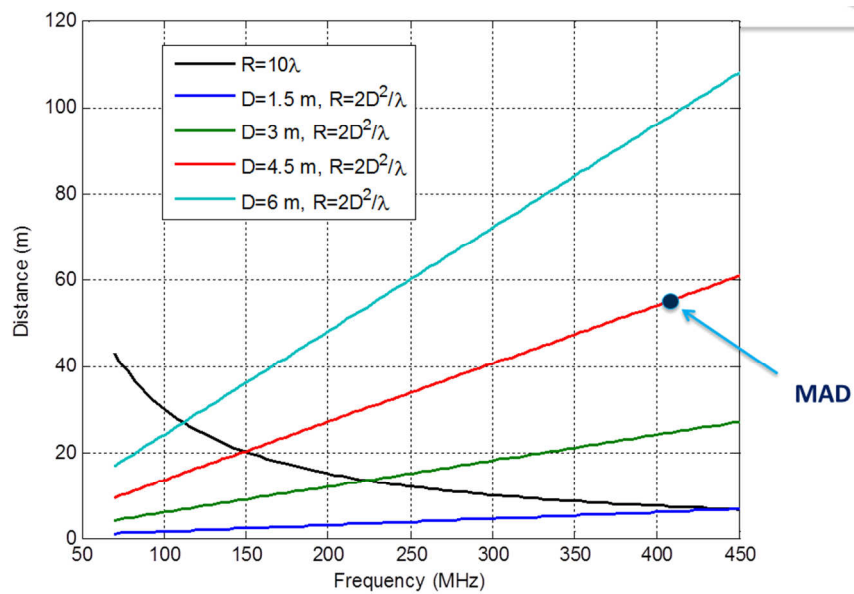


Fig. 12 – Far-field conditions as function of the frequency, for different array sizes.

## 4 – Analogue signal equalization

The coarse analogue signal power level equalization has been performed in order to assure the backend operation in the linear region (backend dynamic range from about -30 dBm to +10 dBm) in the expected MAD-2 conditions. The signal levels have been adjusted to ensure a power of 0dBm for all the ADC inputs when the UAV flight above the array zenith at the height of 60 m. This equalization required a spectrum analyzer working in conjunction to an in-house software controlling the carrier boards of the BEST receivers (Fig. 13) with a minimum step of 0.5dB.



Fig. 13 – (left) Spectrum analyzer and (right) the user interface controlling the carrier boards.

The ADC bits representing the signal power from each antenna was monitored in real-time for the verification of the ADC output (Fig. 14).

| HPOL | BITS | dBm    | VPOL | BITS | dBm    |
|------|------|--------|------|------|--------|
| H001 | 7.26 | -12.68 | V001 | 9.38 | 0.0819 |
| H002 | 7.39 | -11.88 | V002 | 9.46 | 0.5213 |
| H003 | 7.01 | -14.17 | V003 | 9.37 | 0.0043 |
| H004 | 6.83 | -15.28 | V004 | 9.37 | 0.0257 |
| H005 | 6.90 | -14.86 | V005 | 9.40 | 0.1909 |
| H006 | 6.77 | -15.65 | V006 | 9.45 | 0.4913 |
| H007 | 6.81 | -15.40 | V007 | 9.41 | 0.2656 |
| H008 | 7.29 | -12.50 | V008 | 9.42 | 0.3279 |
| H009 | 6.93 | -14.66 | V009 | 9.36 | -0.040 |

2013-10-17 09:12:52.748530 UTC

Fig. 14 – Screenshot of the real-time monitor of the ADC bits with the corresponding received powers

The stationary flight was divided in two parts, one for each polarization:

1 – Stationary position (0 m, 0 m, 60 m) duration 240 s, Tx compass = 0°, flight ID 1xyV

2 – Stationary position (0 m, 0 m, 60 m) duration 240 s, Tx compass = 90°, flight ID 1xyH

The UAV transmission was also used for the verification of the expected minimum and maximum analogue signal levels. The adopted flying strategy was a “L” shape trajectory with change of the Tx dipole from 0° to 90°, for the measurement of both polarizations along their E-planes. With the height of 60 m, the 75 m

length of each trajectory side allowing the beam exploration till about  $\theta = 40^\circ$ . The measured analogue levels were in good agreement with the simulations taking into account the both the path loss and the Tx and Rx calculated beam patterns.

UAV programmed trajectory (in the ENU reference frame):

Flight ID 2xyV

1 – Stationary position (0 m, 75 m, 60 m) duration 30 s, Tx compass =  $0^\circ$

2 – Trajectory (0 m, 75 m, 60 m)  $\rightarrow$  (0 m, 0 m, 60 m), speed = 2 m/s, Tx compass =  $0^\circ$

3 – Stationary position (0 m, 0 m, 60 m) duration 30 s, Tx compass =  $0^\circ$

Flight ID 2xyH

4 – Stationary position (0 m, 0 m, 60 m) duration 30 s, Tx compass =  $90^\circ$

5 – Trajectory (0 m, 0 m, 0 m)  $\rightarrow$  (-75 m, 0 m, 60 m), speed = 2 m/s, Tx compass =  $90^\circ$

6 – Stationary position (-75 m, 0 m, 60 m) duration 30 s, compass =  $90^\circ$

## 5 – Amplitude calibration

The amplitude coefficients were calculated from the observed power ratios respect a reference antenna that, in our case, was the central element of the array (V005/H005). The relationship between the received signal amplitude and the auto-correlation counts was established theoretically and then verified injecting signals of different known powers to the backend. The amplitude coefficients were estimated in order to minimize the differences between received and theoretical power ratios of each array element respect to the reference antenna. The theoretical power ratios were calculated taking into account both the antenna embedded radiation patterns obtained from CST simulations and the Tx antenna pattern and the signal path loss from UAV position data.

A stationary flight of the UAV was chosen for the estimation of the amplitude coefficients:

1 – Stationary position (0 m, 0 m, 60 m) duration 30 s, Tx compass =  $0^\circ$  (for V polarization), ID 3xyV

2 - Stationary position (0 m, 0 m, 60 m) duration 30 s, Tx compass =  $90^\circ$  (for H polarization) , ID 3xyH

The obtained amplitude coefficients, respect that of the reference antenna, are listed in Table 4.

| Antenna ID | Coeff. | Antenna ID | Coeff. |
|------------|--------|------------|--------|
| H001       | 1.39   | V001       | 1.22   |
| H002       | 1.22   | V002       | 1.12   |
| H003       | 1.17   | V003       | 1.32   |
| H004       | 1.22   | V004       | 1.17   |
| H005       | 1.00   | V005       | 1.00   |
| H006       | 1.16   | V006       | 1.09   |
| H007       | 1.20   | V007       | 1.26   |
| H008       | 1.13   | V008       | 1.10   |
| H009       | 1.31   | V009       | 1.21   |

Table 4 – Relative amplitude coefficients for the H and V polarizations. The reference element is H005/V005.

The amplitude calibration was then verified performing a new UAV stationary flight (ID 4xyV and 4xyH) after the introduction of the calibration coefficients (Fig. 15). In the specific case of the MAD backend, the amplitude calibration coefficients have to be multiplied by a constant depending on the firmware design and its parameters (FFT-shift, quantization level, etc.). In MAD-2 the value of constant was set to 3.5 in order to guarantee the system linearity at the expected signal levels.

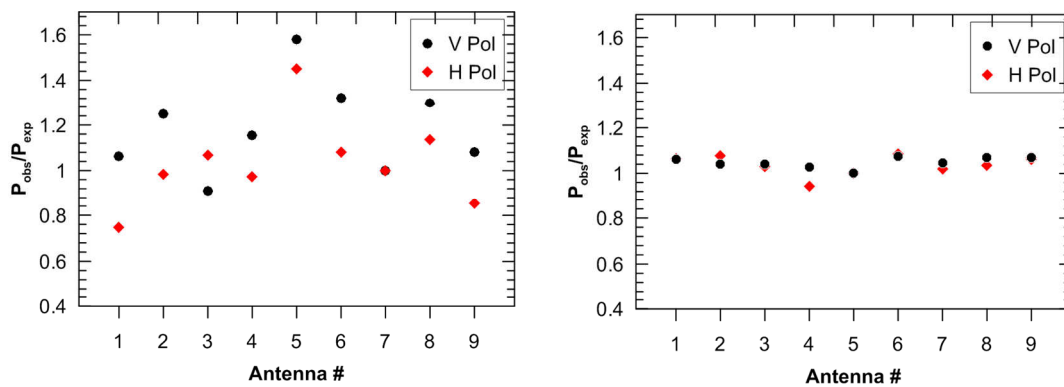


Fig. 15 – (left) power ratios between observed and expected values before and (right) after the amplitude calibration for each individual antenna.

A zoomed plot of the autocorrelations without integration (Fig. 16) shows that some levels are missing. Further investigation demonstrated that this is a normal effect of the discrete signal.

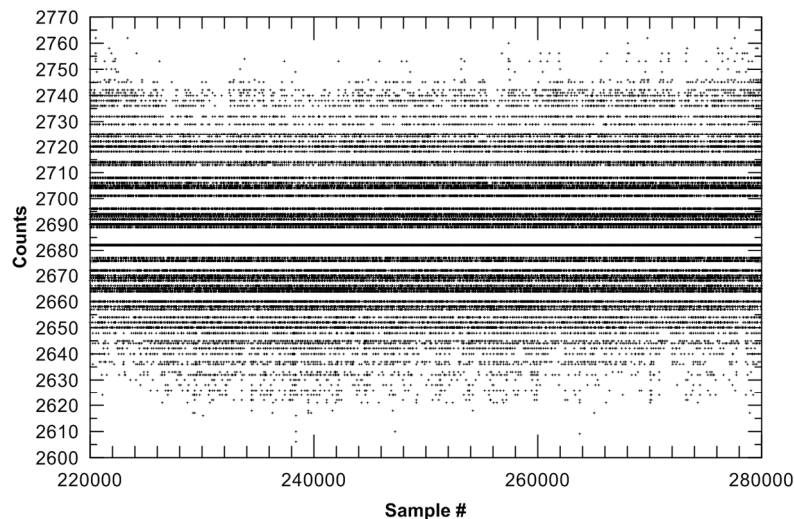


Fig. 16 –Autocorrelation (60000 samples) of the V005 element acquired during the stationary flight 311V

Note that the correlator, in this case, performed only multiplications between the output data from the channelizer (PFB + FFT) without integration.

## 6 – Phase calibration

For the phase calibration, we selected a proper subset of 8 baselines (Table 5 and Fig. 17) among the 36 independent ones for each polarization, in order to increase the phase measurement accuracy by maximizing the fringe frequency pattern on the UAV trajectory. The phase reference antennas were V007 and H009 for the vertical and horizontal polarization, respectively.

| Vertical polarization<br>(E-plane in NS direction) | Horizontal polarization<br>(E-plane in EW direction) |
|--|--|
| V007 – V001  | H009 – H002  |
| V007 – V002  | H009 – H003  |
| V007 – V005  | H009 – H004  |
| V007 – V006  | H009 – H005  |
| V007 – V009  | H009 – H007  |
| V003 – V004  | H001 – H006  |
| V003 – V008  | H001 – H008  |
| V003 – V007  | H001 – H009  |

Table 5 – Baselines selected for the MAD-2 phase calibration

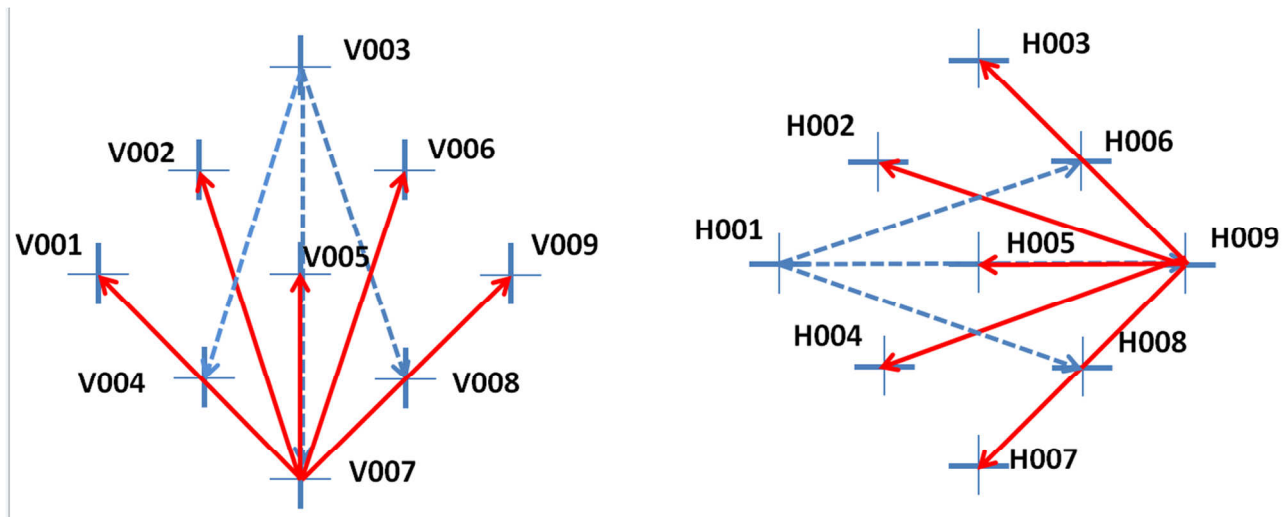


Fig. 17 – Processed baselines for the array phase calibration in vertical (left) and horizontal (right) polarization.

The UAV programmed trajectory (Flight ID 5xyV) for the phase calibration in the V polarization was:

1 – Trajectory (0 m, -50 m, 60 m) → (0 m, 50 m, 60 m), speed = 1.5 m/s, Tx compass = 0°

2 – Stationary position (0 m, 50 m, 60 m) duration 30 s, Tx compass = 0°

3 – Trajectory (0 m, 50 m, 60 m) → (0 m, -50 m, 60 m), speed = 1.5 m/s, Tx compass = 0°

4 – Stationary position (0 m, -50 m, 60 m) duration 30 s, Tx compass = 0°

The same path was used for the verification of the phase calibration in the V-pol (Flight ID 6xyV)

Whereas, for the calibration in the H polarization the UAV scheduled flying path (Flight ID 5xyH) was:

1 – Trajectory (-50 m, 0 m, 60 m) → (+50 m, 0 m, 60 m), speed = 1.5 m/s, Tx compass = 90°

2 – Stationary position (+50 m, 0 m, 60 m) duration 30 s, Tx compass = 90°

3 – Trajectory (+50 m, 0 m, 60 m) → (-50 m, 0 m, 60 m), speed = 1.5 m/s, Tx compass = 90°

4 – Stationary position (-50 m, 0 m, 60 m) duration 30 s, Tx compass = 90°

The same trajectory was adopted to verify the phase calibration in the H-pol (Flight ID 7xyV).

The cross-correlations were acquired by the backend already calibrated in amplitude.

The correlator output for the V006-V007 baseline in the first part of UAV trajectory (SN) is plotted in Fig. 18.

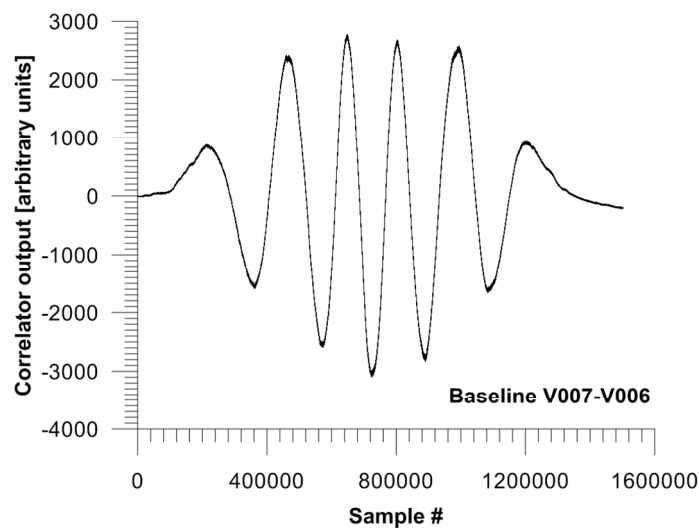


Fig. 18 – Correlator output for the baseline V007-V006 acquired during a calibration flight

A problem in the Total Station synchronization system, occurred during the first part of the MAD-2 campaign, caused a fringe drift even in a short time period. For example, the quick phase drift is clear in Fig. 19 which plots two fringe patterns acquired during the same flight (ID 711H), and then close in time, for the baseline H009-H002.

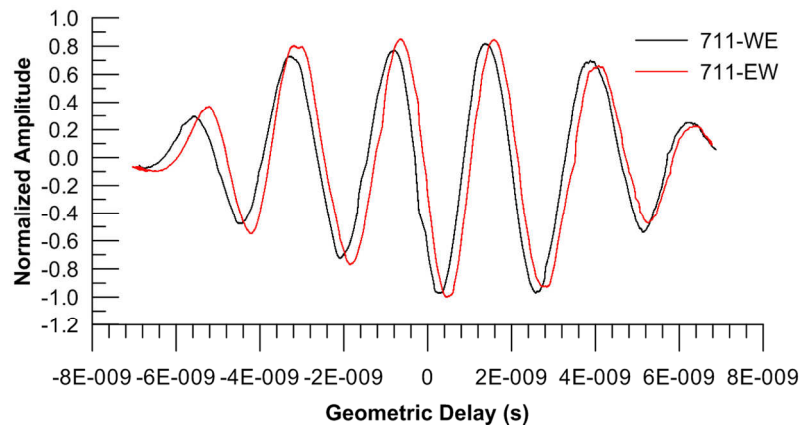


Fig. 19 – Normalized fringe patterns of the baseline H009-H002 acquired along the W-E (black line) and E-W (red line) parts of the flight 711H

The problem of synchronization has been partially fixed resetting the total station clock and then synchronizing it with the GPS before each flight.

Even a slight phase drift still remained after this trick, it was possible to calibrate the array.

The normalized (at maximum) fringe patterns acquired for the subset of 8 baselines (see Fig. 17, left) are shown in Fig. 20.

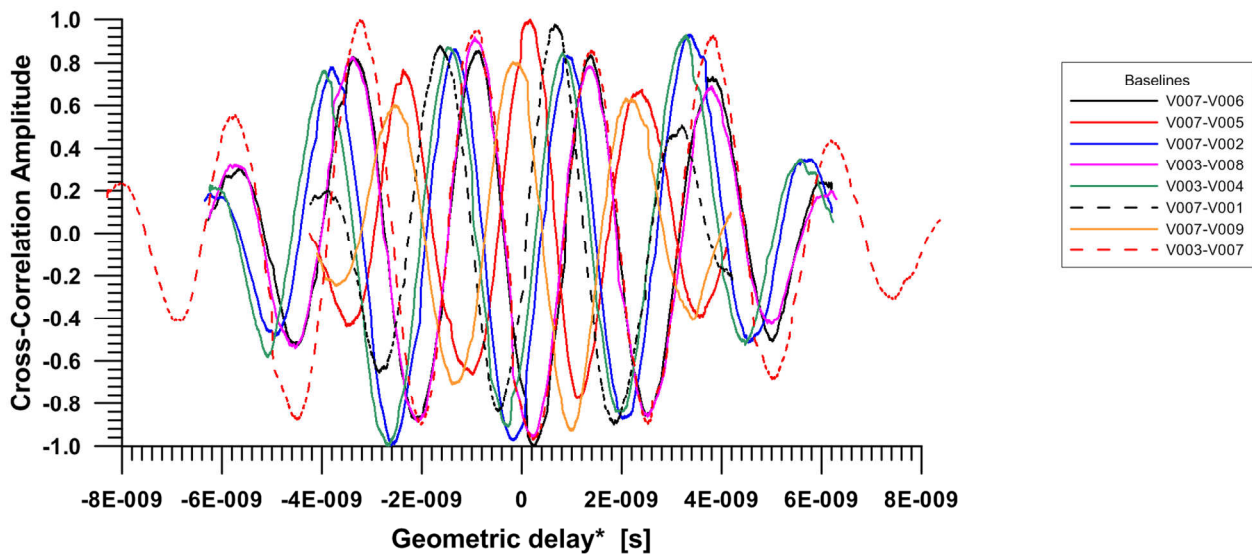


Fig. 20 – Normalized fringe patterns (V-Pol) before the phase calibration

The phase calibration coefficients were obtained from the phase correction values (Table 6) estimated by means of an IDL procedure based on a multi-parametric fringe fitting algorithm.

| Antenna ID             | V001   | V002   | V003   | V004   | V005 | V006   | V007 | V008   | V009   |
|------------------------|--------|--------|--------|--------|------|--------|------|--------|--------|
| Phase correction (deg) | 109.26 | 148.68 | 140.98 | 240.79 | 8.11 | 215.07 | 0.00 | 353.91 | 332.95 |

Table 6 – Phase calibration coefficients for the vertical polarization elements

The fringe patterns acquired after the phase calibration appear to be well aligned with the principal maxima matching the zero geometric delay (see Fig. 21). The antenna V007 is the phase reference element.

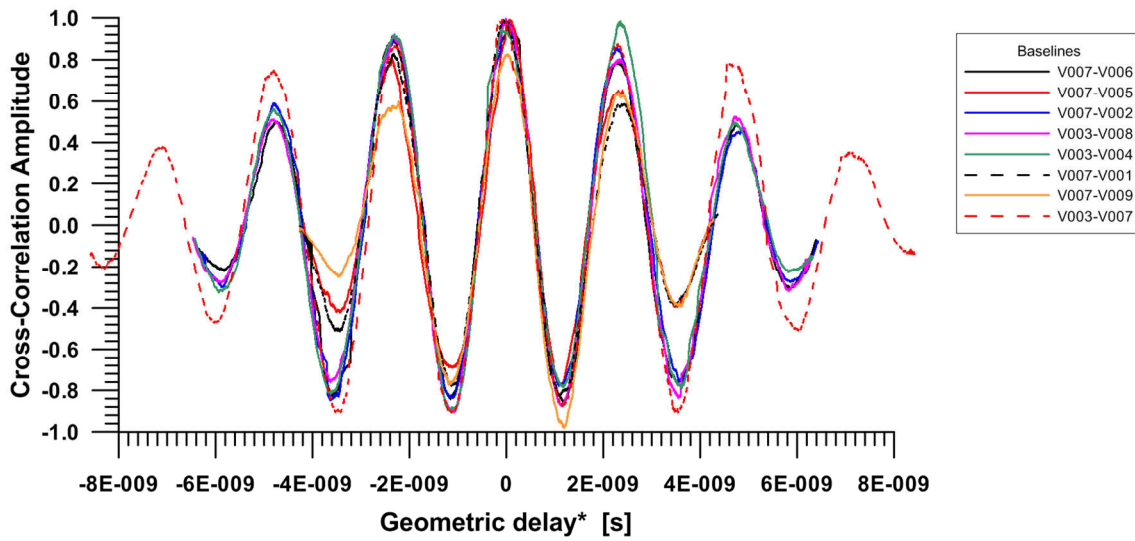


Fig. 21 - Normalized fringe patterns (V-Pol) after the phase calibration

The residual phase errors after the calibration are listed in Table 7.

| Antenna ID                 | V001 | V002 | V003 | V004 | V005  | V006  | V007 | V008  | V009 |
|----------------------------|------|------|------|------|-------|-------|------|-------|------|
| Residual Phase Error (deg) | 1.85 | 0.89 | 0.60 | 1.12 | -0.19 | -0.29 | 0.00 | -0.69 | 0.04 |

Table 7 – Residual of the phase errors for the vertical polarization elements (after calibration)

## 7 - Embedded element patterns

The UAV operates as a controlled far-field radio source in the sky useful for the measurement of the embedded element radiation patterns. Under these conditions, the received power pattern  $P_R(\vec{r})$  along the UAV trajectory, can be described as :

$$P_R(\vec{r}) = P_S \frac{G_S(\hat{r}, \alpha, \beta, \gamma) G_{AUT}(\hat{r})}{\left(\frac{4\pi R}{\lambda}\right)^2} |\hat{p}_S(\hat{r}, \alpha, \beta, \gamma) \cdot \hat{p}_{AUT}(\hat{r})|^2 G_R$$

in which

$\vec{r} = R\hat{r}$  = distance vector

$P_S$  = UAV transmitter power

$G_S(\hat{r}, \alpha, \beta, \gamma)$  = gain pattern of the UAV Tx antenna as function of the direction  $\hat{r}$  and the orientation described by the Euler angles  $\alpha, \beta, \gamma$

$G_{AUT}(\hat{r})$  = gain pattern of the antenna under test

$\hat{p}_S$  and  $\hat{p}_{AUT}$  = polarization vectors of source and antenna under test, respectively

$G_R$  = LNA gain and cable losses

The UAV Tx position and orientation affect the receiver power pattern and therefore the reconstruction of the Rx antenna power pattern  $G_{AUT}(\hat{r})$  from the received power  $P_R(\vec{r})$  requires a proper deconvolution technique.

Since auto-correlations are proportional to the received power, the correlator output can be used to determine the element patterns along the UAV flying path.

During MAD-2, autocorrelations were acquired in a quasi E-plane for both polarizations with the following UAV trajectories:

Vertical polarization E-Plane path (Flight ID 5xyV and 6xyV):

1 – Trajectory (0 m, -50 m, 60 m)  $\rightarrow$  (0 m, +50 m, 60 m), speed = 1.5 m/s, Tx compass = 0°

2 – Trajectory (0 m, +50 m, 60 m)  $\rightarrow$  (0 m, -50 m, 60 m), speed = 1.5 m/s, Tx compass = 0°

Horizontal polarization E-Plane path (Flight ID 6xyH and 7xyH):

1 – Trajectory (-50 m, 0 m, 60 m)  $\rightarrow$  (+50 m, 0 m, 60 m), speed = 1.5 m/s, Tx compass = 90°

2 – Trajectory (+50 m, 0 m, 60 m)  $\rightarrow$  (-50 m, 0 m, 60 m), speed = 1.5 m/s, Tx compass = 90°

It should be pointed out that all the UAV trajectories described in this report are those programmed in the UAV navigation system, but the real flight path can be quite different to the theoretical one due to both errors of the onboard navigation GPS and local wind conditions at the flight altitude. However the UAV is autonomously tracked with the Total Station therefore the real path is known. The normalized autocorrelations as a function of time elapsed from the initial waypoint are shown from Fig. 22 to Fig. 24. These plots are referred to the first part of the scheduled trajectories, i.e. from S to N for the V-Pol and from W to E for the H-Pol.

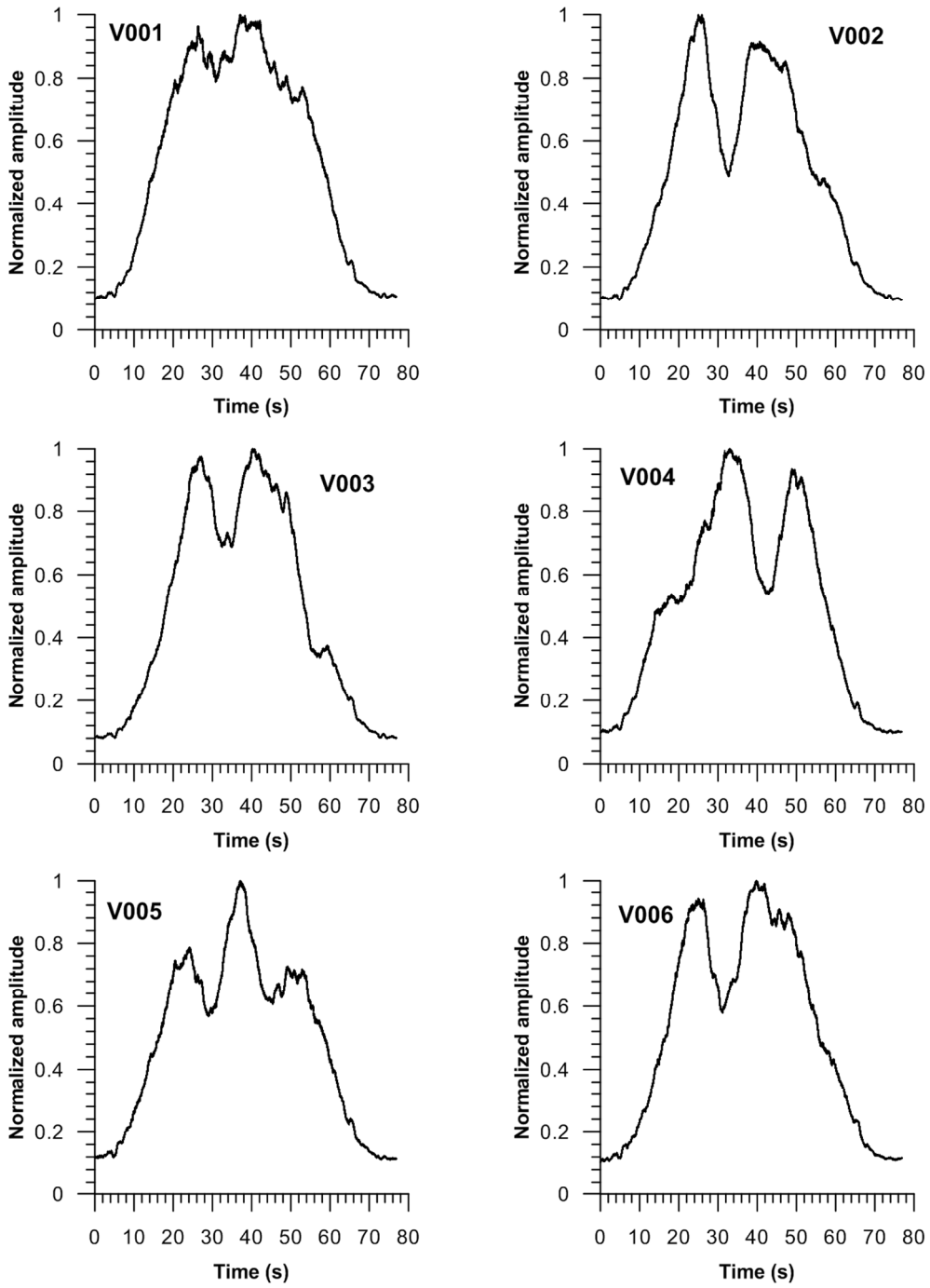


Fig. 22 – Normalized autocorrelations along a quasi E-plane for the elements from V001 to V006

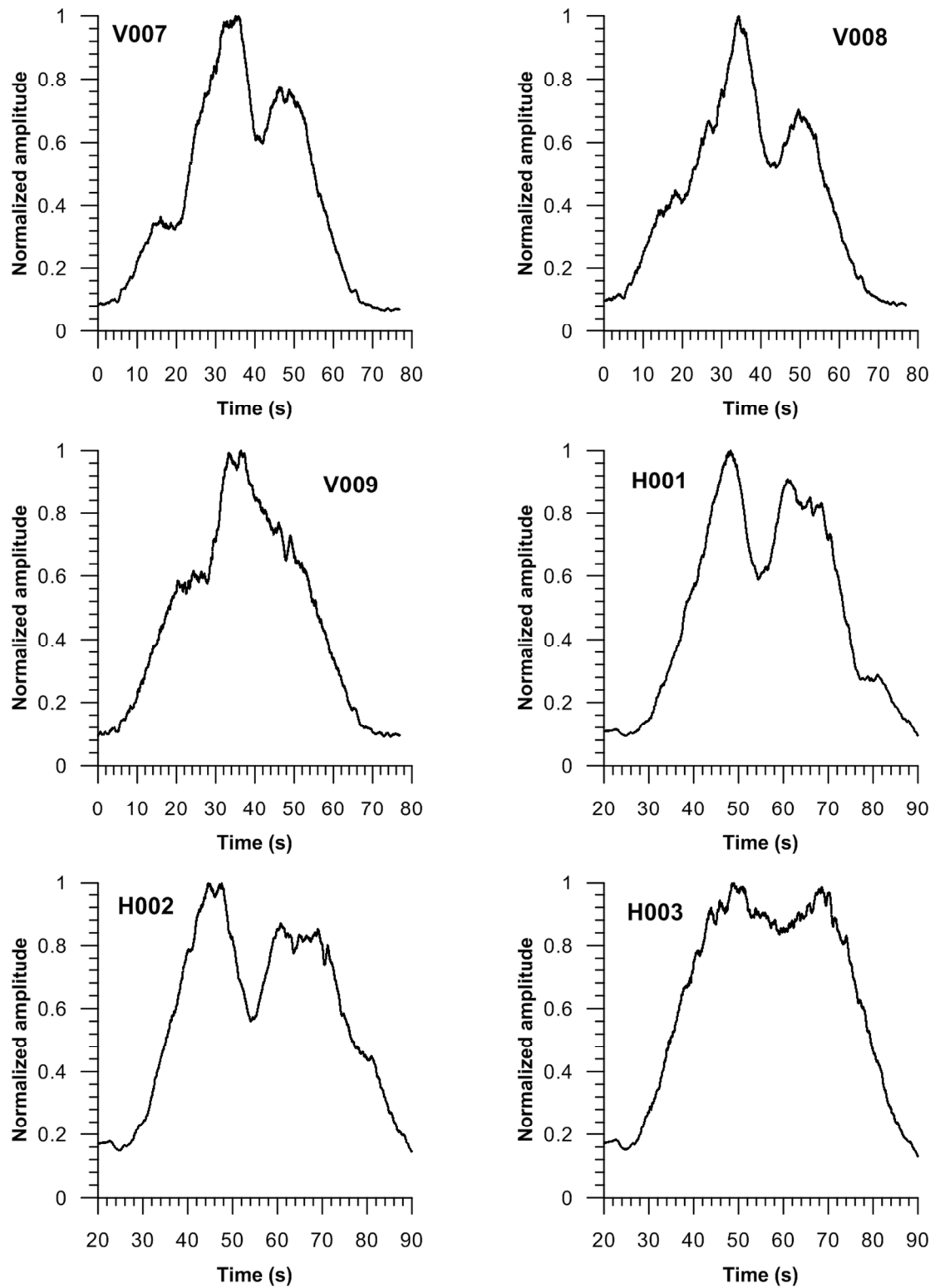
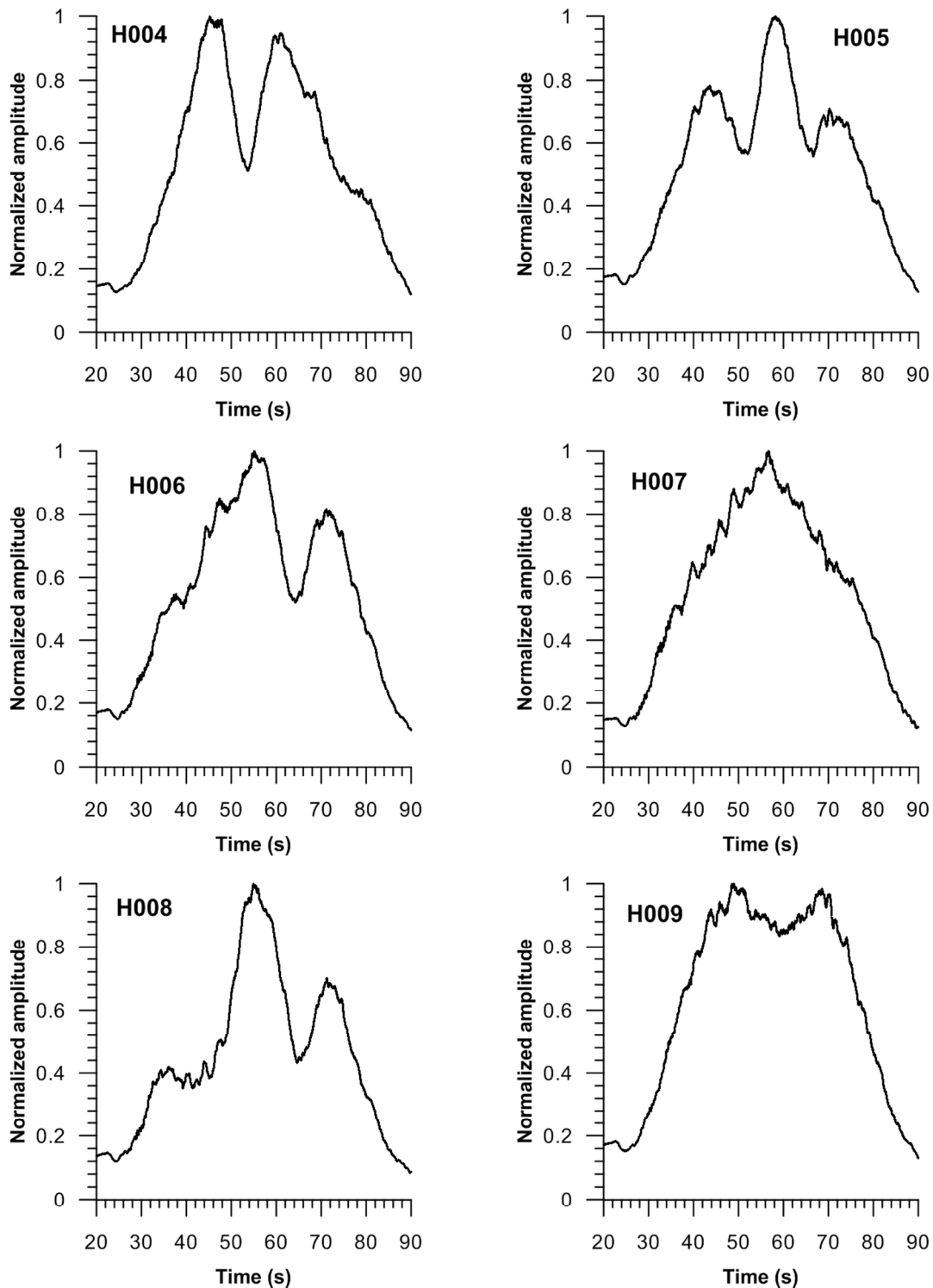


Fig. 23 - Normalized autocorrelations along a quasi E-plane for the elements from V007 to V009 and from H001 to H003



**Fig. 24 - Normalized autocorrelations along a quasi E-plane for the elements from H004 to H009**

It should be pointed out that the patterns appear to be quite different to each other depending on their different position in the array. This is related to the interaction between the array elements (mutual coupling) as well to the influence of the surrounding environment.

The embedded element patterns have been obtained applying the deconvolution procedure to the autocorrelations. Then the patterns have been compared with the electromagnetic simulation performed by CST. The simulated patterns result to be in very good agreement with the observed ones (see Fig. 25 and Fig. 26). The discrepancy between simulations and measurements is about 1 dB. Such an error is probably

due to the measurement field conditions where big scatterers, as the NS-arm of the Northern Cross, were relatively close to MAD. All the MAD-2 measurement were performed for the Copolar component only. This is the reason that measurement/simulation B-port are not plotted in the graphs below.

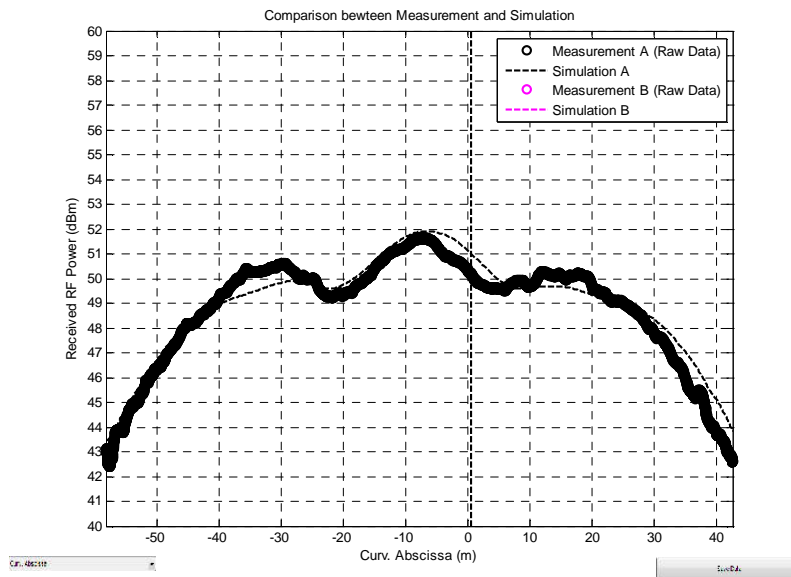


Fig. 25 – Embedded element pattern (E-Plane) comparison for the central element between measurement (solid line) and simulations (dashed line)

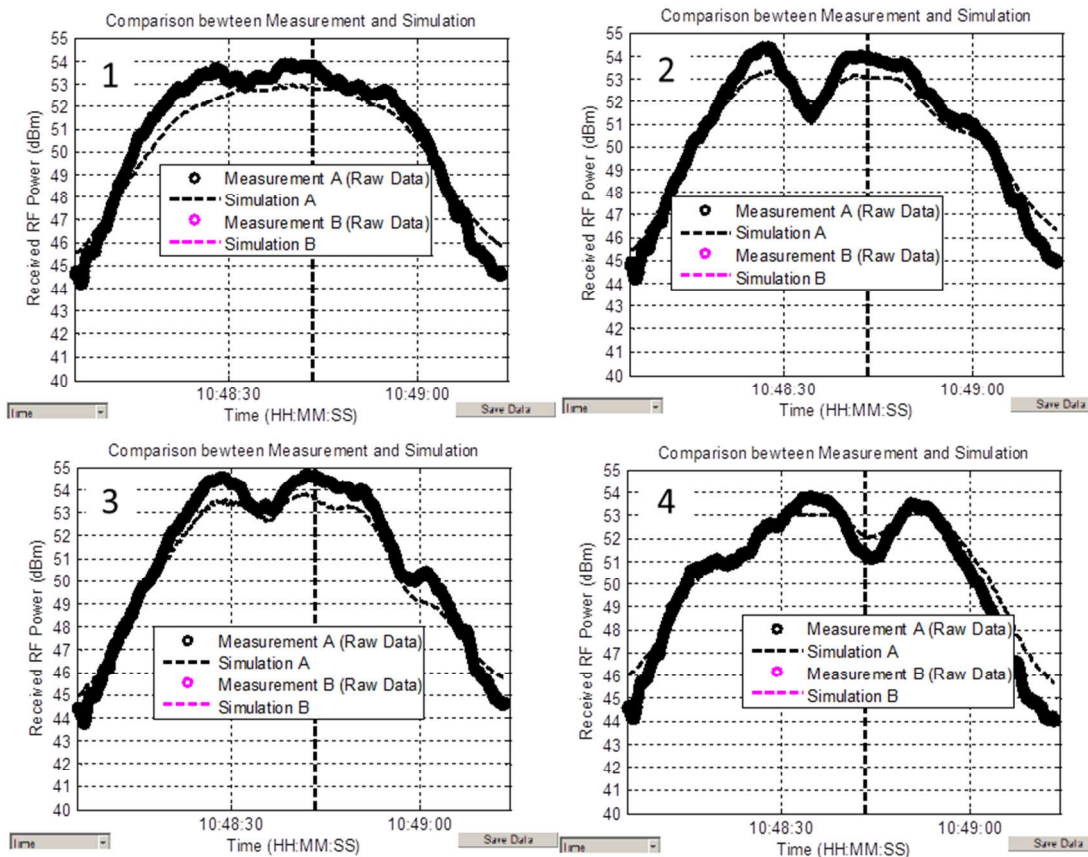


Fig. 26 – Comparison between the embedded patterns for the array elements 1-4: measurement (solid line) and simulations (dashed lines)

## 8 – Array beam

The digitally-formed array pattern has been measured with the UAV system. The digital beamforming has been performed in three different conditions:

- Before phase calibration
- Array partially calibrated
- Array fully calibrated

The array beam in H-pol (quasi E-plane) before phase calibration has been measured during the flight 711H with the UAV flying along a W-E path. The normalized array beam is shown in Fig. 27.

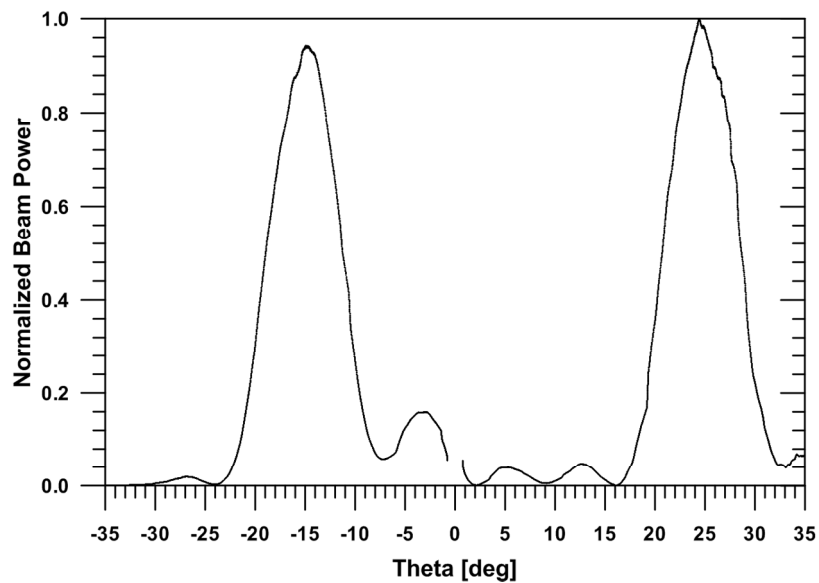


Fig. 27 – Array pattern in H-Pol (quasi E-Plane) of the uncalibrated array

The discontinuity in the beam pattern curve near  $\vartheta = 0^\circ$  is due to the real UAV trajectory did not pass precisely to the array zenith. Even if the digital beam was theoretically steered toward  $\vartheta = 0^\circ$ , the real beam was not pointed toward the desired direction (zenith). Moreover, the double peak is caused by grating lobes, that in a regular array as MAD, are very strong.

The array beam of the partially calibrated array was measured during the first part of the MAD-2 campaign, when the synchronizing problem of the total station prevented an accurate calculation of the phase calibration coefficients. The normalized array beam measured in V-pol (quasi E-plane) is shown in Fig. 28.

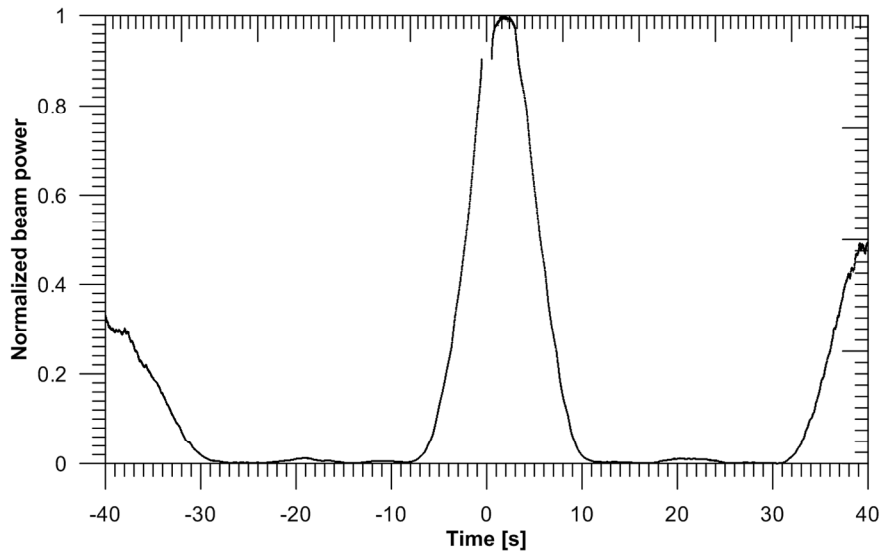


Fig. 28 - Array pattern in V-Pol (quasi E-Plane) of the partially calibrated array

In spite of the phase calibration errors of some tens of degrees, the array beam is nearly pointed toward the zenith, with a pointing error of about  $2^\circ$ .

Finally, after the synchronization problems was partially fixed, the digital array beam for the well calibrated array has been measured (Fig. 29).

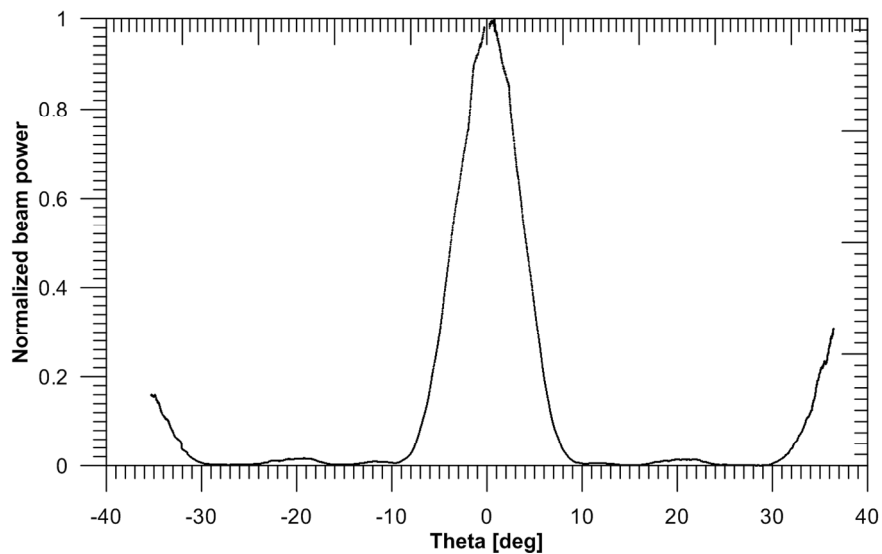


Fig. 29 - Array pattern in V-Pol (quasi E-Plane) of the fully calibrated array

The trajectory programmed on the UAV navigation system was the following (ID 9xyV):

Trajectory (0 m, -50 m, 70 m)  $\rightarrow$  (0 m, +50 m, 70 m), speed = 1.5 m/s, Tx compass =  $0^\circ$

In this case the array beam is correctly pointed toward the desired direction (pointing error  $< 1^\circ$ ). The same pattern, after deconvolution, was compared with simulations (Fig. 30). This comparison shows an impressive agreement between measurement and simulation. The half power beam width is about  $8^\circ$ , with high levels at  $\vartheta \cong \pm 35^\circ$  related to the grating lobes.

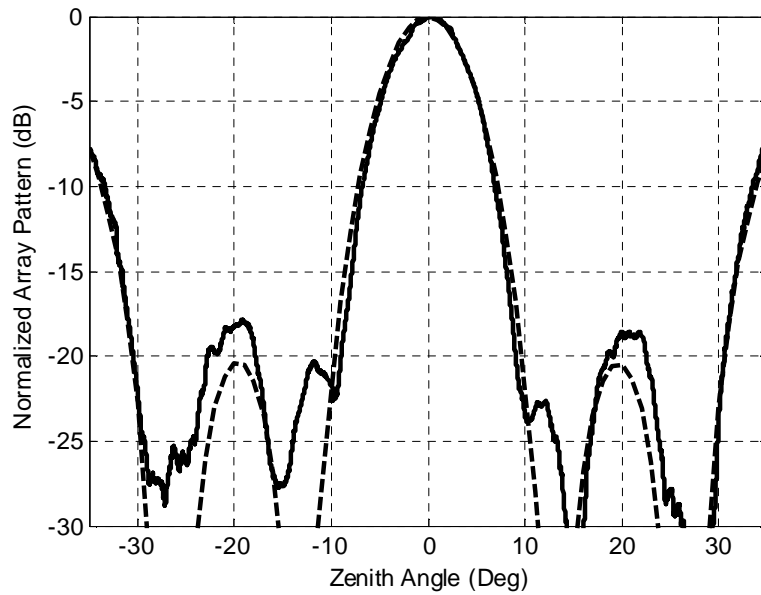


Fig. 30 – Array pattern in V-Pol (quasi E-plane): measurement (solid line) and simulation (dashed line)

## 9 – Conclusions

The MAD-2 measurement campaign has confirmed the effectiveness of the UAV as a far-field source in a small low-frequency array in order to:

- Measure the embedded element patterns and the array pattern in real operative conditions
- Verify the effects of the environment on the element patterns comparing them with electromagnetic simulations
- Calibrate the array in phase and amplitude
- Validate the backend and the acquisition system

Moreover MAD-2 has drawn the attention to the:

- Synchronization problem of the total station synchronization that has to be fixed, as instance installing a differential GPS aboard the UAV, in order to improve the measurements / calibration accuracy
- Precision in the z-coordinate measurement by aerial photogrammetry

## Acknowledgements

We wish to thank Irene Aicardi, Horea Bendea, Germano Bianchi, Claudio Bortolotti, Alessandro Cattani, Corrado Contavalle, Adila Fatobeni, Franco Fiocchi, Federica Govoni, Paolo Maschio, Matteo Murgia, Fabio Paonessa, Marco Piras, Marco Poloni, Juri Roda, Mauro Roma, Simone Rusticelli, Paolo Zacchiroli, Kristian Zarb Adami, Jack Hickish, Griffin Foster and Alessio Magro for their technical support.

## 10 – List of abbreviations

ADC = Analog to Digital Converter

BEST-2 = Basic Element for SKA Training 2

CST = Computer Simulation Technology<sup>®</sup>

ENOB = Effective Number of Bits

FFT = Fast Fourier Transform

FPGA = Field Programmable Gate Array

GPS = Global Positioning System

IF = Intermediate Frequency

LFAA = Low Frequency Aperture Array

LO = Local Oscillator

MAD = Medicina Array Demonstrator

PFB = Polyphase Filter Bank

PPS = Pulse per Second

RF = Radio Frequency

RX = Receiver

ROACH = Reconfigurable Open Architecture Computing Hardware

SKA = Square Kilometre Array

TX = Transmitter

UAV = Unmanned Aerial Vehicle

## 11 – References

[1] G. Virone et al. - “Antenna Pattern Verification System Based on a Micro Unmanned Aerial Vehicle (UAV)”, IEEE, Antennas and Wireless Propagation Letters, vol. 13, 2014

[2] J. Monari et al., “Aperture Array for Low Frequency: the Vivaldi solution” – IEEE International Conference on Electromagnetics in Advanced Applications (ICEEA) – Torino, September 9-13, 2013

[3] F. Chiabrando et al. – “Direct Photogrammetry Using UAV: Tests and First Results” - ISPRS Archives, vol. XL-1, 2013

[4] G. Pupillo et al. – “Calibration of aperture array receivers based on unmanned aerial vehicle”, 2<sup>nd</sup> ERATEC Workshop on Calibration of multi-beam receivers, Bologna, October 28-29, 2013

[5] G. Virone et al. – “UAV-based Radiation Pattern Verification for a Small Low-Frequency Array” – IEEE International Symposium on Antennas and Propagation, USNC-URSI National Radio Science Meeting 2014, Memphis, USA, July 6-12, 2014

## 12 – Appendix A

### Flight ID code

The flight ID code is composed of four alphanumerical characters. The first character indicates the type/purpose of the flight, the second character is the day number of the test, the third is the sequence number of that flight and the last one is “V” or “H” in case of V-pol or H-pol acquisition, respectively.

Moreover, if a flight is divided in different parts, the suffix “\_%n” is added to the ID code, where %n identifies the trajectory branch (e.g. flight 221\_1V and 221\_2V).

| ID code | Flight type/purpose  |
|---------|--|
| /       | Array photogrammetry   |
| 1xy     | Stationary flight for the analogue equalization  |
| 2xy     | “L” shape trajectory for the verification of the minimum and maximum analogue levels along the E-planes of the H-pol and V-pol.  |
| 3xy     | Stationary flight for the evaluation of the amplitude coefficients   |
| 4xy     | Stationary flight for checking the amplitude calibration   |
| 5xy     | <ul style="list-style-type: none"> <li>- Rectilinear flight in NS direction</li> <li>- Evaluation of the phase calibration coefficients for V-pol</li> <li>- Embedded pattern measurement for V-pol along the E-plane</li> </ul> |
| 6xy     | <ul style="list-style-type: none"> <li>- Rectilinear flight in NS direction</li> <li>- Check of the phase calibration in V-pol</li> <li>- Embedded pattern measurement for V-pol along the E-plane</li> </ul>                    |
| 7xy     | <ul style="list-style-type: none"> <li>- Rectilinear flight in EW direction</li> <li>- Evaluation of the phase calibration coefficients for H-pol</li> <li>- Embedded pattern measurement for H-pol along the E-plane</li> </ul> |
| 8xy     | <ul style="list-style-type: none"> <li>- Rectilinear flight in EW direction</li> <li>- Check of the phase calibration in V-pol</li> <li>- Embedded pattern measurement for H-pol along the E-plane</li> </ul>                    |
| 9xy     | “X” shape flight for the array beam measurement along E and H planes of the V-pol  |
| Axy     | “X” shape flight for the array beam measurement along E and H planes of the H-pol  |

x = day number of test (starting from 1)

y = flight sequence number (from 1 to 9)